RSC Advances

ROYAL SOCIETY OF CHEMISTRY

PAPER

View Article Online
View Journal | View Issue

Check for updates

Cite this: *RSC Adv.*, 2020, **10**, 5540

Photochemical *anti–syn* isomerization around the –N–N═ bond in heterocyclic imines†

Michal Hricovíni,[a] James Asher[b] and Miloš Hricovíni *[c]

Received 19th December 2019
Accepted 28th January 2020

DOI: 10.1039/c9ra10730d

rsc.li/rsc-advances

EPR and NMR experiments on a quinazolinone-based Schiff's base in DMSO solution showed that irradiation with UV light (365 nm) leads to photochemically-induced isomerization from the *anti*- to the higher-energy *syn*-form around the –N–N═ linkage. The *anti*- to *syn*-isomerization was relatively fast, and the maximum amount of conversion detected (25%) was reached within 10 min; thermodynamic equilibrium re-established itself in about 15 min. DFT calculations were performed on the investigated compound and small model systems, and reproduced the experimental fact of the *anti*-conformer being lower in energy than the *syn*. Theoretical analysis of excited states, including visualisation of natural transition orbitals, identified possible pathways for *syn–anti* isomerisation, although the details vary with π-system size, making the use of small models of limited utility. The investigated compound probably isomerises through the third singlet excited state (S_3), a π–π* excitation, relaxing through S_2, also a π–π* state.

1. Introduction

The effects of ultraviolet (UV) and optical (vis) radiation on molecular structures have been widely studied, as energy transfer in the UV/vis region plays an important role in a number of chemical and biological processes.[1,2] The transformation from the energetically more favourable *anti*-isomer to the *syn*-isomer by UV/vis excitation has been found to occur in many organic molecules.[3,4] Systems possessing a double bond between two atoms with bulky substituents tend to undergo an isomerisation process,[5] but then relax back to the more stable isomer by thermal relaxation or when exposed to a particular wavelength of light.[6,7] The re-isomerisation process can sometimes proceed very rapidly, especially in the case of highly-conjugated systems with small substituents and an aliphatic backbone.[8] On the other hand, some systems relax significantly more slowly and relax to the lower-energy isomer only after days or months.[9]

The are many photochemically-induced biological processes associated with nitrogen-containing heterocyclic compounds, such as Schiff's bases.[10,11] These compounds have shown a broad spectrum of applications in pharmacology and medicine,[12] but they also serve as catalysts,[13] optical materials and dyes,[14,15] and play an important role in inorganic biochemistry.[16,17] Depending on their structure, compounds of this type have a wide range of biological activities and are well-known for their antibiotic activities, including anticancer, antiviral and anticonvulsant effects.[18,19] These activities can be increased by coordination with various metal ions, and complexes with metal ions are currently being used as successful models of biologically-active agents and precursors for pharmaceutical development.[20,21] Quinazoline and quinazolinones also belong to the class of nitrogen-containing heterocyclic compounds which possess significant therapeutic potential, having antimicrobial,[22] anticancer,[23] anti-inflammatory,[24] or other[25] beneficial effects. Unlike the previously mentioned Schiff's bases,[26] however, little is known about their photochemical properties. Only a few photochemical studies have been performed dealing with quinazolinones.[27–29] Recently, photochemically-induced isomerization of a quinazolinone derivative containing a large π-system (consisting of two C_6 rings linked by a reduced quinazolinone moiety and a N_{ring}–N═CH–$C_{aromatic}$ bridge) has been described.[30] Unlike previous studies describing isomerization around a C–C linkage[27–29] or a N═N linkage (in the case of azobenzene and its derivatives),[31,32] isomerization proceeded around a N–N linkage in the N–N═CH array of this system. This finding prompted us to study similar molecular systems, and in this paper we present experimental data and in-depth theoretical analysis to identify the excited states that are likely to be involved in the photochemically-induced isomerization process.

The subject of this paper is a Schiff base possessing a quinazolinone moiety[30,33] (**S1**; Fig. 1), with a series of model compounds **M1–M4** (Fig. 2) also being studied at the

---

[a] Institute of Chemistry, Slovak Academy of Sciences, Dúbravská cesta 9, 845 38 Bratislava, Slovak Republic

[b] Institute of Inorganic Chemistry, Slovak Academy of Sciences, Dúbravská cesta 9, 845 36 Bratislava, Slovak Republic

[c] Institute of Chemistry, Slovak Academy of Sciences, Dúbravská cesta 9, 845 38 Bratislava, Slovak Republic. E-mail: milos.hricovini@savba.sk; Fax: +421-2-5940222; Tel: +421-2-59410323

† Electronic supplementary information (ESI) available. See DOI: 10.1039/c9ra10730d

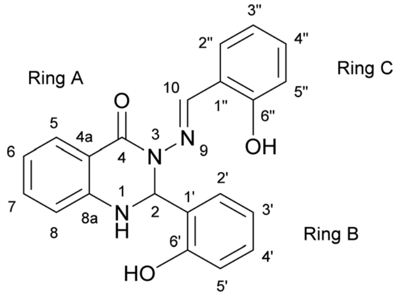

Fig. 1 The structure of Schiff base (**S1**) with atom and ring labelling. The compound is depicted in the *syn*-form.

computational level in order to investigate the photochemical behaviour of the –N–N= linkage. We shall focus on the photoswitching properties of the N–N linkage under UV radiation in DMSO solution. Photochemically-induced *anti*-/*syn*-isomerization around the N–N bond has been analysed by means of UV/vis, EPR, and NMR spectroscopy, complemented by DFT calculations, to understand the photochemistry of the N–N=CH array.

2. Experimental section

2.1. Instruments

Stock solutions of compound **S1** ($c = 1$ mM) in DMSO (SeccoSolv, Merck, Germany) were freshly prepared directly before measurements. The solutions of all spin traps were prepared in dried DMSO (SeccoSolv, Merck, Germany). The spin-trapping agent 5,5-dimethyl-1-pyrroline-*N*-oxide (DMPO; Sigma-Aldrich, Switzerland) was distilled before application, 2,3,5,6-α-(4-pyridyl-*N*-oxide)-*N*-*tert*-butylnitrone (POBN; Sigma-Aldrich, Switzerland) and 2,3,5,6-tetramethylnitrosobenzene (nitrosodurene, ND, Sigma-Aldrich, Switzerland) were used without any previous purification. Saturated ND solutions were prepared before the experiments due to the limited solubility of ND in DMSO. Solutions of the investigated compounds with a spin-trapping agent present (DMPO, POBN and ND) were mixed before the EPR measurements in the presence of air. The final mixtures were immediately transferred to a quartz flat cell (WG 808-Q, Wilmad-LabGlass, USA) and directly irradiated at 20 °C in a standard rectangular EPR cavity (ER 4102 ST, Bruker, Germany). A monochromatic radiator ($\lambda_{\max} = 365$ nm; Bluepoint LED, Hönle UV Technology, Germany) was used as a source of UV light. The presence of reactive paramagnetic intermediates generated upon UV/VIS irradiation was monitored by cw-EPR spectroscopy using a Bruker EMX Plus (Germany) spectrometer at 9.5 GHz (X-band). The *g*-values were determined by the built-in magnetometer. The *in situ* EPR spectra were then processed and simulated by the WinEPR (Bruker, Germany) and Winsim 2002 (NIEHS, USA) software.

High-resolution NMR spectra of **S1** were recorded in a 5 mm cryoprobe on a Bruker Avance III HD (Germany) spectrometer at 14 T. One-dimensional 600 MHz ^{1}H and 150 MHz ^{13}C NMR spectra, together with two-dimensional COSY, NOESY, ROESY, HSQC, and HMBC, enabled determination of the ^{1}H and ^{13}C chemical shifts (referenced to internal TMS) and ^{1}H–^{1}H intramolecular NOEs. Variable-temperature measurements (from 20 °C up to 65 °C) were performed in order to monitor the variations in the chemical shifts of the labile protons. Samples were then exposed to high-powered (500 μW cm^{-2} at a distance of 10 cm) UV irradiation (365 nm) using a UV lamp (Krüss Optronics, Germany) equipped with VIS filters which effectively filter the visible light from the tubes. The irradiation times were 2, 4, 6, 8, 10, 20, 30 and 60 minutes. 1D and 2D NMR spectra of the irradiated samples were then measured at 14 T under the same experimental conditions as before UV light exposure.

2.2. Computational details

Calculations were performed on the smaller model systems (**M1–M4**) and on the full Schiff's base (**S1**) with Gaussian 09 (ref. 34) using the ωB97XD[35] functional. The basis sets chosen were LanL2DZ,[36] 6-311++G(2d,2p)[37] and DGDZVP[38] combined with the SMD model[39] for the approximation of the DMSO solvent environment. The functional ωB97XD was employed in all types of calculations as it was previously found suitable for calculating similar organic systems.[40] The convergence criteria were set to tight unless otherwise noted, using (for **S1** only) an ultrafine integration grid. Additionally, some calculations with CCSD[41] and basis sets cc-pVDZ[42] and cc-pVTZ[43] were performed for comparison (with normal, not tight, convergence criteria). Excited state calculations – both single-point and, in some cases, optimisation – were performed using TD-DFT[44] and, for benchmarking, EOM-CCSD.[45] Additionally, CAS-SCF calculations were performed for benchmarking purposes, using OpenMolcas.[46] Only singlet excited states were considered.

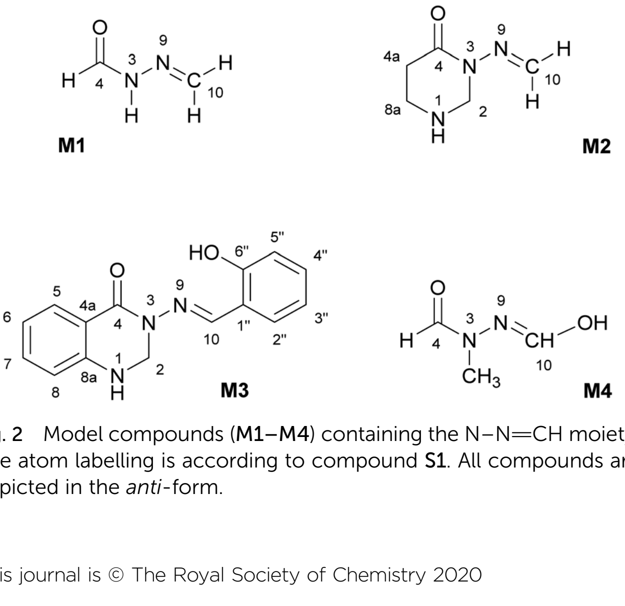

Fig. 2 Model compounds (**M1–M4**) containing the N–N=CH moiety. The atom labelling is according to compound **S1**. All compounds are depicted in the *anti*-form.

3. Results and discussion

3.1. EPR spectroscopy

The first step in analysis of the compounds was to apply EPR spin-trapping techniques to study the photoinduced generation of reactive paramagnetic intermediates on UV irradiation. Multiple spin-trapping agents (DMPO, POBN, ND) were used in order to detect and identify reactive species. Exposure of **S1** to UV caused immediate generation of the EPR signals of the corresponding spin-adducts. Photoactivation of **S1** in aerated DMPO/DMSO solution resulted in the generation of a twelve-line signal ($a_N = 1.276$ mT, $a_H^\beta = 1.033$ mT, $a_H^\gamma = 0.137$ mT; $g = 2.0059$) attributed to the $^\bullet$DMPO–O_2^- adduct (Fig. 3a). The spin-adduct $^\bullet$DMPO–O_2^- is formed by the interaction of the excited states of **S1** with atmospheric oxygen *via* consecutive electron-transfer reactions.[47] In addition, other oxygen-centred radical adducts were found, namely $^\bullet$DMPO–OCH_3 ($a_N = 1.304$ mT, $a_H^\beta = 0.844$ mT, $a_H^\gamma = 0.189$ mT; $g = 2.0059$, 37%) and other alkoxy radicals ($^\bullet$DMPO–OR′) ($a_N = 1.362$ mT, $a_H^\beta = 1.175$ mT; $g = 2.0058$, 3%). The formation of the aforementioned spin-adducts is associated with the interaction of *in situ* formation of $O_2^{\bullet -}$ with the DMSO solvent.[48]

Application of POBN resulted in the formation of an EPR signal (Fig. 3b) wherein two oxygen-centred adducts with very similar coupling constants were identified. The hyperfine coupling constants indicated the adduct $^\bullet$POBN–OCH_3 ($a_N = 1.358$ mT, $a_H^\beta = 0.169$ mT, $g = 2.0059$) to be the dominant product in the system (98%). The other adduct, $^\bullet$POBN–O_2^- ($a_N = 1.479$ mT, $a_H^\beta = 0.219$ mT, $g = 2.0059$), represented about 2% of the total radical concentration. Furthermore, carbon-centred adducts were also investigated. The spin-trapping agent nitrosodurene, suitable for the detection of carbon-centred radicals, unambiguously confirmed the production of methyl radical, forming $^\bullet$ND–CH_3 ($a_N = 1.394$ mT, $a_H^\beta(3H) = 1.27$ mT; $g = 2.006$, 100%) (Fig. 3c) and no other radicals.

The presence of reactive intermediates in the system gives us information on the photochemical behaviour of compounds upon irradiation. The detected radicals arise from consecutive reactions between superoxide (produced by electron transfer from excited-state **S1**) and the solvent.[49,50] The resulting spin-adducts cannot be directly used for complete structural analysis, but are sufficient to confirm the presence of radical intermediates.

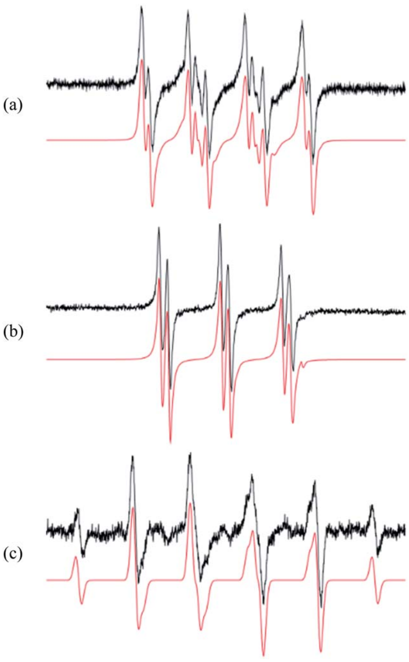

Fig. 3 The experimental (–) and simulated (–) EPR spectra monitored upon UV irradiation ($\lambda_{max} = 365$ nm, irradiance: 13 mW cm^{-2}) of **S1** in the aerated DMSO solutions containing the spin trapping agents: (a) DMPO (SW = 8 mT); (b) POBN (SW = 8 mT); (c) ND (SW = 8 mT).

Photoexcitation is in many cases associated with chemical bond rearrangement, especially in conjugated systems.[3,51] Many studies[52–54] have described these processes, wherein structural changes in the excited state allows the system to undergo photochemical isomerization *via* several pathways.[55–57] The NMR and DFT calculations were therefore focused on the analysis of structural changes in **S1** that may plausibly be induced by the photochemical processes.

3.2. NMR spectroscopy

High-resolution ^{1}H NMR spectra of the newly-synthesized compound **S1** in DMSO is shown in Fig. 4a. The analysis of the solution structure confirmed that the pure *anti*-isomer had been obtained from the synthesis. UV irradiation (365 nm) in DMSO at room temperature led to considerable changes in the NMR spectra, and new resonances arose whose intensities increased with UV irradiation time (Fig. 4b). 2D HSQC and NOESY spectra, as well as comparison with our previous data,[30] confirmed that these resonances originated from the *syn*-isomer, indicating *anti*–*syn* photoisomerization. Formation of the *syn*-isomer was relatively fast with respect to the previously-analysed analogues,[30] and the maximum amount of conversion (25%) was observed within 10 min. The re-establishment of thermodynamic equilibrium (at room temperature), *i.e.* reversion to the *anti*-form, took about 15 min. Critically, experiments under inert atmosphere (to exclude atmospheric oxygen) made no visible difference to the spectra, making it unlikely that isomerisation proceeds through a radical mechanism involving electron transfer.

The temperature coefficients of the –N_3–N=C(H) protons and OH protons were determined from the chemical shift variations collected in high-resolution NMR spectra between 20 °C and 65 °C for the *anti*-isomer (Table 1). The coefficients for

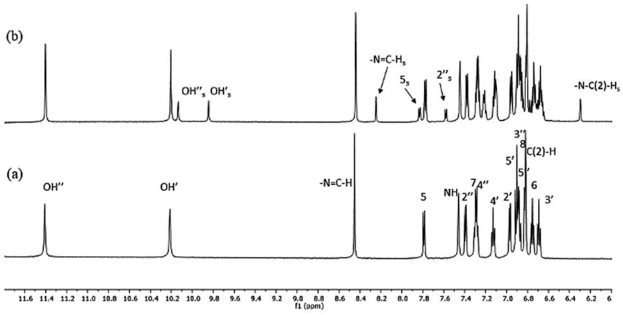

Fig. 4 (a) High-resolution 600 MHz ^{1}H NMR spectrum of **S1** in DMSO at 25 °C. (b) ^{1}H spectra of **S1** obtained after UV irradiation ($\lambda_{max} = 365$ nm) after 10 min of irradiation. Smaller signals (marked with subscript s) belong to the *syn*-isomer, which formed upon irradiation; assignments without indices belong to the main form (*anti*-isomer).

Table 1 Temperature dependence of the chemical shifts of $-N{=}C(H)$ and $-OH$ protons in **S1**

			(20 °C)	(25 °C)	(35 °C)	(45 °C)	(55 °C)	(65 °C)	ppb K^{-1}
S1	*anti-*	$-OH'$	10.233	10.203	10.142	10.080	10.020	9.958	−6.11
		$-OH''$	11.434	11.409	11.353	11.299	11.246	11.193	−5.36
		$N_3{-}N{=}CH$	8.441	8.454	8.477	8.499	8.522	8.542	−2.24
		$-NH$	7.484	7.460	7.408	7.357	7.305	7.254	−5.11

the OH protons for **S1** were −5.36 and −6.11 ppb K^{-1} and indicated that the OH groups are involved in intramolecular H-bonds with comparable strengths. Similarly, data for the $-N_3-N{=}C(H)$ protons (−2.24 ppb K^{-1}) and the NH protons (−5.11 ppb K^{-1}) indicated that these groups are also involved in weak intra- and intermolecular H-bonds,[58] as seen previously.[30] However, fast reversion to the *anti*-isomer prevented us from performing temperature-dependent NMR measurements for the *syn*-isomer.

3.3. DFT calculations

3.3.1. Geometry. Density functional theory at the ωB97XD/6-311++G(2d,2p) level, with the SMD model for the approximation of DMSO environment, was used for theoretical analysis of the energies and the geometry of both isomers (Fig. 5).

The relative energies between the *anti*- and *syn*-forms for all model compounds **M1–M4** and **S1** are listed in Table 2 and the selected geometry parameters are in Table 3. The energy difference between the *anti*- and *syn*-forms is 7.56 kJ mol^{-1} (3.00 mH) for **S1** (for comparison with **M1–M4**, see Table 2) and is comparable to those previously analysed.[30,59,60] Comparison of **M2** with **M3** indicates that the energy gap between the two isomers is slightly decreased by extending the π-system with additional benzene rings; on going from **M3** to **S1**, additional interactions between ring B and ring C (presumably dispersion and/or electrostatic effects) then stabilise the *anti*-form, increasing the energy gap again. However, as noted in Section 3.3.2, the DFT calculations may not be completely reliable for energy differences.

The bond lengths in the aromatic rings of both the *anti*- and *syn*-forms **S1** were generally in the range of 1.38–1.41 Å (Table 3) and correspond to those in structurally-related molecules.[61,62] Virtually no differences were observed in the $C_{10}-C_{1''}$ bond lengths (1.53–1.57 Å), which are comparable with single bonds in similar systems.[63] The N_3-N_9 bond has partial double-bond character (1.360 Å for *anti*- and 1.386 Å for the *syn*-isomer in **S1**) as it partakes in a delocalised system stretching from the ring A to ring C (Fig. 5). The effect of the delocalisation along the $C_4-N_3-N_9-C_{10}$ array is clearly visible from the calculated bond length values. The C_4-N_3 bond is shortest for **M1** and longest for **S1**, indicating the elongation of this bond with addition of the substituents (Table 3, row 5). Incorporation of the heterocyclic moiety (**M2**) to the structure of **M1** caused elongation of the bond (1.380 *vs.* 1.356 Å). A significant effect is also seen after addition of the aromatic ring C to the carbon atom C_{10}; there is a visible zigzag double-bond formation in the $C_4-N_3-N_9-C_{10}$ linkage, where the N_3-N_9 bond was shortened and the N_9-C_{10} bond was prolonged (Table 3, rows 3 and 4, respectively). On the other hand, the differences between **M3** and **S1** are minimal; the presence of the ring B has a negligible effect on the $C_4-N_3-N_9-C_{10}$ moiety (Fig. 1). Due to the absence of heterocyclic or aromatic rings in the **M4** structure, different structural changes were seen in this derivative, namely a significant prolongation of the N_3-N_9 bond (the longest of all derivatives; Table 3) as the result of the shortening of both the N_9-C_{10} (the shortest out of all compounds, Table 3) and the C_4-N_3 bonds. This effect is caused by the conjugation of the non-bonding pairs from the nearby electron-donating OH group with the N_9-C_{10} linkage. This is also confirmed by the $N_3-N_9-C_{10}$ bond angle, which is more than 2° narrower (3° for *syn*-) compared to **M1** (Table 3, first row). The effect of OH group is further discussed in Section 2.4.3.

The computed values of the $N_3-N_9{=}C_{10}$ bond angles vary by less than 5°, *i.e.* the system is quite rigid. Similar differences between *anti*- and *syn*-forms are also seen for the $C_4-N_3-N_9$ bond angle (up to 10°). As seen from the calculated dihedral angles, the $C_4-N_3-N_9{=}C_{10}$ torsion angle – representing planarity of the system around the N_3-N_9 moiety – is more sensitive to the presence of functional groups, including aromatic systems. Whereas the angle is about 13° away from planar for the *anti*-isomer, a significant deviation from planarity is observed in the case of *syn*-isomer (approx. 57°); this will be discussed in Section 3.3.3 below. As expected, the torsion angle for $N_3-N_9{=}C_{10}-C_{1''}$ is close to 0° (varying by up to 2°) for **S1**. The difference between **M3** and **S1** is minimal, indicating that ring B

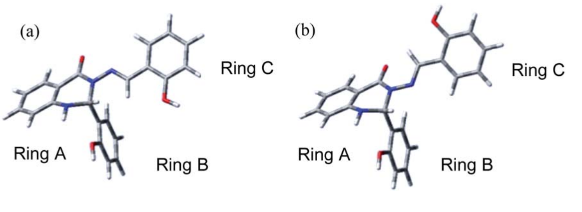

Fig. 5 DFT-optimised geometries of compound **S1**: (a) *anti*-isomer, (b) *syn*-isomer.

Table 2 DFT-computed energy differences (kJ mol^{-1}) between the *anti* and *syn*-forms for all compounds using ωB97XD functional, 6-311++G(2d,2p) basis set and SMD solvent model (DMSO)

Compound	**M1**	**M2**	**M3**	**M4**	**S1**
$\Delta E_{syn} - \Delta E_{anti}$	7.88	6.09	4.99	2.39	7.56

Table 3 Selected optimised bond lengths (Å), bond angles (degrees) and torsion angles (degrees) for **M1–M4** and **S1** obtained by DFT calculations at the ωB97XD/6-311++G(2d,2p) using SMD solvent model (DMSO)

		M1		**M2**		**M3**		**M4**		**S1**	
		anti-	*syn-*	*anti-*	*syn-*	*anti-*	*syn-*	*anti-*	*syn-*	*anti-*	*syn-*
Bond length	$C_{1''}–C_{6''}$	—	—	—	—	1.410	1.409	—	—	1.410	1.410
	$C_{10}–C_{1''}$	—	—	—	—	1.458	1.453	—	—	1.457	1.453
	$N_3–N_9$	1.365	1.371	1.365	1.375	1.357	1.387	1.374	1.402	1.360	1.386
	$C_{10}–N_9$	1.267	1.272	1.270	1.272	1.278	1.280	1.265	1.268	1.278	1.279
	$C_4–N_3$	1.356	1.356	1.380	1.368	1.385	1.385	1.358	1.349	1.388	1.384
	$C_2–N_3$	—	—	1.463	1.471	1.459	1.462	1.449	1.447	1.458	1.459
Bond angle	$N_3–N_9–C_{10}$	120.7	116.5	120.1	123.1	122.7	117.5	118.6	113.4	122.5	117.9
	$N_9–C_{10}–C_{1''}$	—	—	—	—	119.4	120.7	—	—	119.4	120.3
	$C_4–N_3–C_2$	—	—	123.8	122.3	121.3	118.2	121.2	122.5	122.5	120.8
	$C_{8a}–N_1–C_2$	—	—	110.4	109.8	116.7	115.2	—	—	116.8	116.3
	$N_1–C_2–N_3$	—	—	110.4	110.2	109.0	108.0	—	—	108.2	107.4
	$C_4–N_3–N_9$	121.6	130.8	115.8	126.5	114.9	119.8	117.1	120.8	115.0	120.6
	$C_{1'}–C_2–N_3$	—	—	—	—	—	—	—	—	112.4	113.4
Torsion angle	$C_4–N_3–N_9–C_{10}$	−180	0	−170.9	14.8	−165.7	58.9	−180	−67.1	−167.3	57.4
	$C_2–N_3–N_9–C_{10}$	—	—	3.4	−177.7	−1.5	−156.8	0	131.1	1.3	−151.9
	$N_3–N_9–C_{10}–C_{1''}$	—	—	—	—	−179.5	−178.0	—	—	179.9	−178.1
	$N_9–C_{10}–C_{1''}–C_{6''}$	—	—	—	—	−2.2	1.0	—	—	−2.3	2.0
	$N_3–C_2–C_{1'}–C_{2'}$	—	—	—	—	—	—	—	—	−9.3	−11.7
	$N_1–C_2–N_3–C_4$	—	—	−21.8	−31.1	−41.8	−53.6	—	—	−38.7	−48.1

has no effect on the $N_3–N_9{=}C_{10}–C_{1''}$ the dihedral angle. The effect of ring B was seen only for dihedral angle $N_1–C_2–N_3–C_4$ (varying by approx. 5°), as expected.

3.3.2. Benchmarking.

Various calculations were performed on **M1** for benchmarking purposes, with some performed on **M2** and **M4** for comparison purposes; full details are given in the ESI.† The variation of the **M1** ground-state energy with the $C_4–N_3–N_9{=}C_{10}$ torsion angle (Fig. S1†) is qualitatively similar for all methods. (We will henceforth label this torsion angle as $\phi_{(C–N–N–C)}$ for simplicity.) The ωB97XD functional with the smaller basis – labelled WB-L2 – overestimates the height of the energy barrier, but WB-6+ (the larger basis) gives more reasonable results. The *syn–anti* energy difference is also more accurate with WB-6+ than WB-L2. However, the results for **M2** and **M4** show that the *syn–anti* energy difference is not too reliable even with the larger basis set. The overestimate of energy barriers by WB-L2 is a general trend, though; and, as discussed below, WB-L2 fails to describe certain features of the ground-state energy profile for both **M2** and **M4**.

The vertical excitation energy curves for the first three singlet excited states of **M1** are compared to EOM-CCSD and CASSCF results in the ESI.† The energy curves look somewhat similar for CC-TZ and WB-6+; the CASSCF results depend on the excitations included, but frequently differ in having a small peak in the 120–150° region for the first excited state, and possibly the second. TD-DFT and CASSCF have the same state ordering for the first three excited states (in order, excitations from HOMO-1, HOMO, and HOMO-2 to LUMO); EOM-CCSD has the 2nd and 3rd of these swapped around, and accordingly has the oscillator strengths swapped as well (TD-DFT has ES1 and ES3 as dark states; EOM-CCSD has ES1 and ES2 as dark states. CASSCF, however, predicts all three states to be dark.) Overall, the WB-6+ level seems to be mostly accurate enough for our purposes, but should be treated with caution regarding the *syn–anti* energy difference.

Calculations at EOM-CCSD level have also been performed for the first excited state of **M2**; these are in approximate agreement with TD-DFT results (see ESI†).

3.3.3. Ground-state energy profile.

For **M1**, both the molecule and its energy profile with respect to $\phi_{(C–N–N–C)}$ are symmetric; however, **S1** is a rather asymmetric molecule with a very asymmetric energy profile. This is shown in Fig. 6, top, where the energy profiles of **S1** and **M1**, **M2** and **M3** are compared (at WB-6+ level). The C_4N_2 ring present in **M2** introduces a major part of the asymmetry, as there is steric repulsion between the Schiff's base CH_2 group and the ring CH_2 group, with the latter being locked into an asymmetric position by being part of the ring. This causes asymmetry in the energy maxima, with one peak at ∼−115° and one at ∼+120°, the former being 2.1 kJ mol^{-1} (0.8 mH) higher. This asymmetry increases in **M3** and **S1**. In addition, there is a small shoulder around 0°, which pushes the *syn-* energy minimum to about 50–60°, visible for **M2**, **M3** and **S1**; we will comment on this below.

The difference between **S1** and **M3** is the aromatic ring B, which does not participate in the large π-system, and whose principal effect on the energy curve will be steric, electronic and possibly dispersion interactions with ring C on the other side of the N–N bond. Fig. 6, bottom, shows the energy curves of **S1** and **M3**, adjusted so the *syn* minima coincide; the difference made by the extra $–C_6H_4OH$ group is to lower the energy of the *anti-*conformer in **S1** and also to shift the position of the peak at ∼−100 to −110° in the direction of the *anti-*conformer. Calculations with the ωB97X functional,[64] *i.e.* without dispersion corrections, are also shown in Fig. 6, bottom (adjusted relative

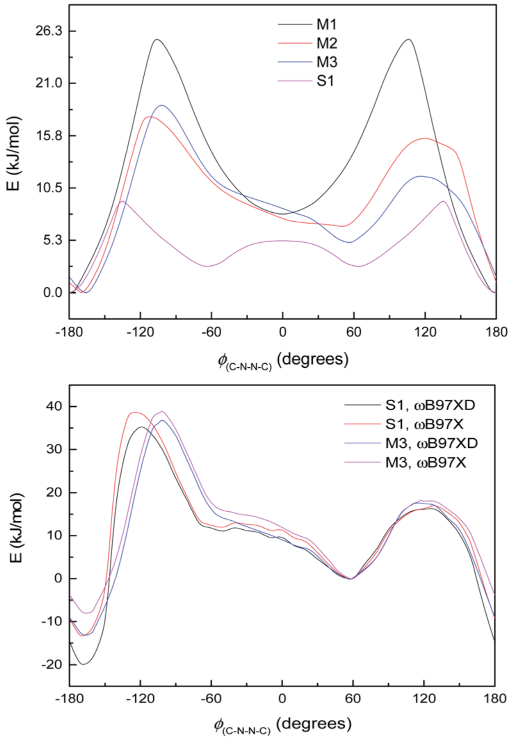

Fig. 6 Ground state energy curves (kJ mol^{-1}) against C_4–N_3–N_9–C_{10} dihedral angle for **S1** and model systems. Top: energy profiles for **S1** and **M1**, **M2**, and **M3** (zeroed to lowest energy point on curve). Calculated at the ωB97XD/6-311++G(2d,2p) (WB-6+) level. Bottom: **S1** and **M3** (zeroed to *syn* minimum). Calculated at the ωB97XD/6-311++G(2d,2p) or ωB97X/6-311++G(2d,2p) level, as specified.

to the *syn*-form); these indicate that the lower energy of the *anti*-conformer is due to dispersion interactions (presumably between rings B and C), although the shift in the peak position remains unexplained.

The small shoulder around 0° in **S1** and **M3** (Fig. 6, bottom), which pushes the *syn* minimum to >50°, is visible as a peak in its own right in the energy curve for **M4** (Fig. 7, top), which lacks an extended π-system and has an OH group attached directly to the Schiff's base moiety. **M4** displays minima at ±60° and 180°, with a small peak at 0° and larger peaks at ±135° (Fig. 7, top). This suggests that the peak (or shoulder) at 0° arises from resonance structures with negative charge at the Schiff's base nitrogen (Fig. 7, bottom). **M4**, with a nearby electron-donating OH group, naturally shows such effects most strongly; in the larger π-systems of **S1** and **M3**, where the OH group is further away and the peaks at ±100–130° are asymmetric, the 0° peak is merely a shoulder to whichever peak is closer to 0°. In **M2**, which has no electron-donating group, this effect is weaker: the shoulder is less pronounced, and disappears when a polarisable continuum model (PCM) is used instead of SMD. (PCM encourages charge separation less than SMD, so would understate the effects of charge-separated resonance structures. However, PCM only removes this peak/shoulder for **M2**; it is found even with PCM for **M3**, **M4** and **S1**.)

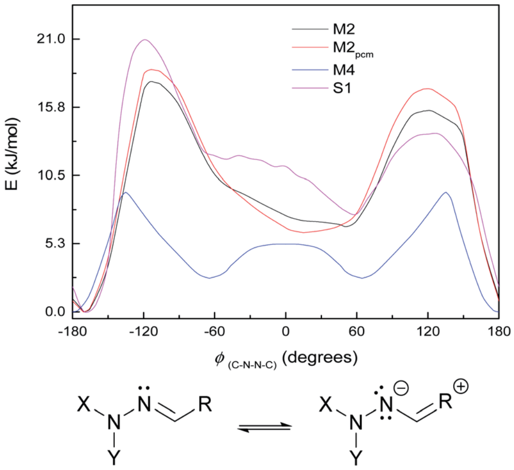

Fig. 7 Top: ground-state energy curves for **S1**, **M2**, **M4**, and **M2**$_{pcm}$ against $\phi_{(C-N-N-C)}$. Bottom: resonance structure with negative charge on Schiff's-base nitrogen.

(We note that we chose **M4** as a striking example of this effect; for the system HCO–NH–N═CH–OH, *i.e.* **M4** with CH_3 replaced by H or **M1** with an additional OH, the peak around 0° is present but weaker and noisier. The effect is also seen with NH_2 instead of OH.)

These curves were all calculated at the WB-6+ level (except where noted). It is also notable that the WB-L2 level fails to find the peak/shoulder at 0° for **M2** and **M4**, and does not find a significant shoulder for the larger model systems (see ESI†); it appears that this effect needs a large basis to be treated properly. (This effect is present at CC-DZ level for **M2** and **M4**, so it is not an artefact of the ωB97XD functional.) The appearance of peaks at 0° and a little over 120°, but not at 180°, suggests an explanation of steric repulsion between the C═O group and the electron pairs (two lone pairs, one N–C bond) on sp^3-hybridised N$^-$.

The topic of how the π-system responds to substituents on the aromatic rings (and how this relates to the experimentally-observable properties of differently-substituted Schiff's bases) is an interesting one, and we are preparing a second paper which will discuss the matter in more depth.

3.3.4. Excited states.

In this section, we shall discuss potential energy curves for ground and excited states against the dihedral angle $\phi_{(C-N-N-C)}$. The gap between ground and excited states is, in all cases, far larger than the variation in energy of any one state. This makes graphs difficult to read. All graphs have therefore been adjusted to bring the energy curves closer together. Unadjusted graphs are to be found in ESI (Fig. S5, S8 and S10),† together with tables of calculated excitation energies and oscillator strengths.

Fig. 8 shows the energy curves for the ground state and first three singlet excited states of **M1**, the most basic model system. (These are energy curves using the ground-state geometries rather than geometries reoptimised for the excited states.) The excited states have kinks or discontinuities around 107° for reasons that are discussed in the ESI (section Excited states):†

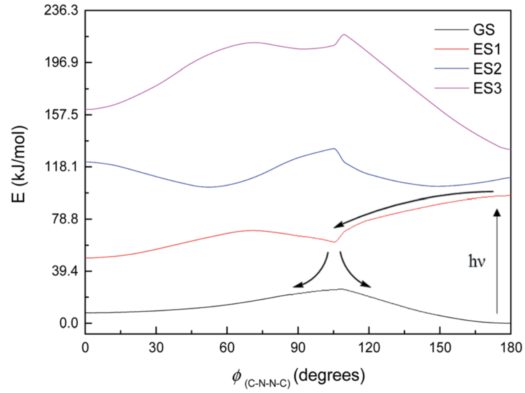

Fig. 8 Energy curves for the ground state (GS) and first three excited states (ES1–ES3) of **M1**. Relative energies (kJ mol^{-1}) of the states have been heavily adjusted for clarity.

essentially, the ground state has a slightly different character for the ranges 0–107° and 107–180°, and so do the excited states as a result. The first excited state, according to DFT (and EOM-CCSD), has its highest energy at 180°, and its lowest energy at 0°; although as mentioned the CASSCF calculations have 180° as a local minimum and a small peak around 120° (ESI, section Excited states†). Attempted optimisation of the excited states leads to very small energy differences, indicating a conical intersection of ES1 with the ground state across most of the range of $\phi_{(C–N–N–C)}$ – in spite of the large vertical excitation energies and also a conical intersection between the first and second excited states. (The optimisation leads to negligibly small energy differences.)

The first excited state has a vertical excitation energy profile that could lend itself to *anti–syn* isomerisation – generally decreasing in energy from *anti* to *syn* (though as mentioned, CAS-SCF disagrees with TD-DFT and EOM-CCSD on this). (However, the energy profile of the GS-S_1 conical intersection has an energy barrier around 105°, as for the ground state.) The second excited state similarly has an appropriate energy profile, with a local minimum around 120–150° that could relax to the top of the GS energy barrier. However, the oscillator strength for the transition to ES1 is very low according to all methods ($f <$ 0.01 for the *anti*-conformer); ES2 is accessible according to TD-DFT ($f = 0.480$) but not CASSCF or EOM-CCSD. Isomerisation would thus require some higher-energy excitation, which would then relax to S_1 and perhaps cross to the other side of the 107° energy barrier before falling through the conical intersection; or could relax to ES2, move to the local minimum around 120–150°, and then relax to ES1 and thence to GS. We note that ES1 arises from an n–π* transition, and ES2 from a π–π* transition; these correspond to HOMO–LUMO or nHOMO–LUMO (according to whether the HOMO or nHOMO are n or π in character; this changes with dihedral angle). ES3 and ES4 are π–π* states. The NTOs for these states are depicted in the ESI (section Excited states).†

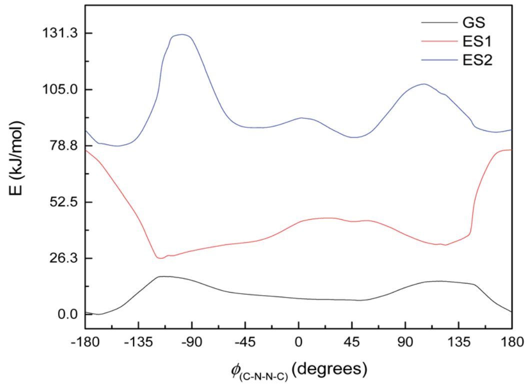

Fig. 9 Ground state (GS) and first two excited states (ES1 and ES2) energy curves for **M2**. Relative energies of the curves have been adjusted for clarity.

This, however, is the simplest possible system. **M2** is slightly closer to the full system, having the C_4N_2 ring but not the extensive π-system. The excited state energy curves for **M2** are shown in Fig. 9. There are significant differences from **M1**: the ES1 state has an energy maximum around 0° (the *syn* conformation), instead of an energy minimum; and ES2 looks more like the ground state than it does in **M1**. More importantly, however, the oscillator strengths are a little higher: still very small for ES1 ($f = 0.035$) but $f > 0.1$ for both ES2 and ES3. (ES3 – data not shown – looks similar to ES3 for **M1**, including a deep

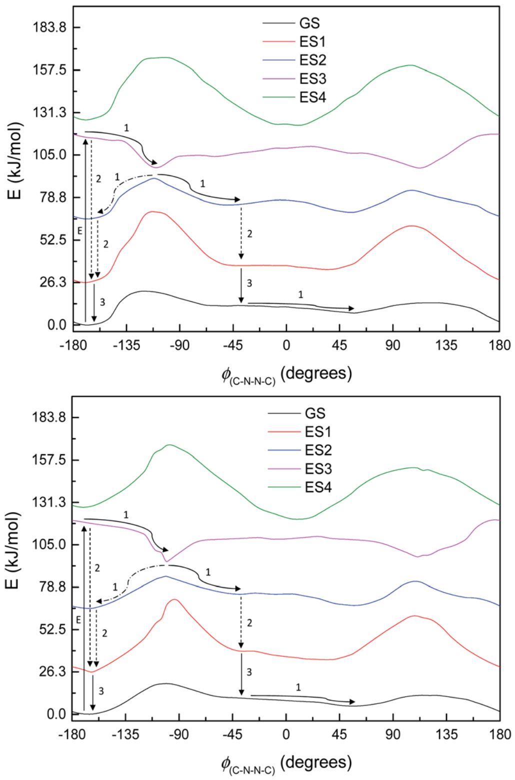

Fig. 10 Energy curves for ground state (GS) and excited states (ES1–ES4) of **M3** (top) and **S1** (bottom) with proposed mechanisms of excitation and deexcitation processes (E – excitation, 1 – structural relaxation, 2 – internal conversion, 3 – emission). Relative energies (kJ mol^{-1}) of the curves have been adjusted for clarity.

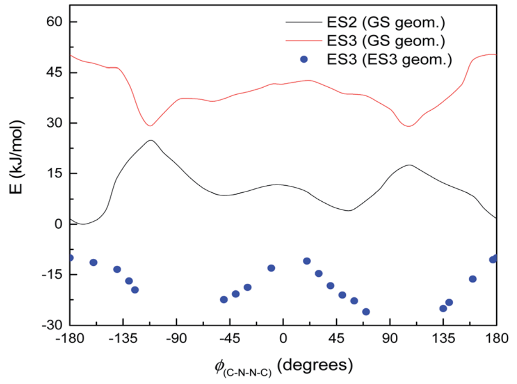

Fig. 11 Excited state energies for **S1**, varying with $\phi_{(C-N-N=C)}$ dihedral angle. Full lines: vertical excitation energies of ES2 and ES3 from ground state. Filled circles: optimised ES3 energies. Gaps around 90 and −90° are due to very low ES2/ES3 energy gaps.

minimum at 180°.) We can imagine a similar mechanism to **M1**: excitation to ES2 and relaxation to ES1 and then GS, with movement to the other side of the energy barrier while in ES1. (Again, there seem to be conical intersections between the states.)

By the time we get to **M3** and **S1**, the situation looks a little different. The π-system is significantly larger, and as a result, there are now three π–π* excitations lying below the n–π* excitation, so the n–π* excited state is now the 4th (ES4), instead of the 1st as seen in **M1**. (The energy curves are shown in Fig. 10; the excited states look very similar for both **M3** and **S1**.) The n–π* excited state energy curve also has minima in-plane and maxima out-of-plane, just like the ground state; it is therefore not expected to play any role in isomerization. (Its oscillator strength continues to be rather low – $f = 0.016$.)

Of the three lower-lying π–π* excited states, the first two have similar energy profiles to the ground state; but the third has an inverted energy profile, and a conical intersection with the 2nd excited state. (These excitations also have moderately high oscillator strengths – 0.478, 0.236, 0.295.) This provides an obvious pathway for photoisomerization, similar to the pathway in the model systems: a molecule excited to ES3 undergoes structural relaxation to the conical intersections at ±90°, and thence to either the *syn-* or *anti*-conformer of ES2, and then undergoes internal conversion (IC) to ES1 (or undergoes IC from ES2 before relaxing to the *syn-* or *anti*-form). Unlike in other systems, however, our proposed isomerisation mechanism would compete with IC, which, after excitation, would relax the molecule to the *anti*-conformer of ES2 and then ES1, preventing isomerisation. These two pathways are labelled in Fig. 10.

Normally in photochemical reactions, IC is fast enough to ensure that only the lowest excited state (of the relevant multiplicity) undergoes any reaction, due to the population of higher excited states diminishing too quickly for reactions to take place; this is the extension of Kasha's rule[65] to photochemistry. However, in cases where either IC is slowed down or the reaction is sufficiently fast, reaction from higher excited states may be seen (see ref. 66 and 67 for an overview). Our suggested mechanism fits the latter criterion: movement down the potential energy slope is simple structural relaxation, without so much as an energy barrier. This would be expected to take place on the timescale of nuclear motion (<1 ps), and thus be competitive with IC. The third excited state has been optimised for much of the $\phi_{(C-N-N=C)}$ curve: Fig. 11 shows the energies, compared to the vertical excitation energies for the 2nd and 3rd excited state. (There are gaps in the energy curve due to the ES2/ES3 energy difference becoming negligible, *i.e.* conical intersection.)

Natural transition orbitals (NTOs) for multiple states of **S1** are shown in Fig. 12.

Our calculations thus indicate that, for these systems, whether photoisomerization involves n–π* excitations or proceeds purely *via* π–π* states is determined by the π-system size – a large enough π-system will have a suitable π–π* excitation lower than the n–π* excitation; furthermore, the n–π* excitation changes its energy profile with size, having a more suitable energy profile for isomerisation in the smaller systems

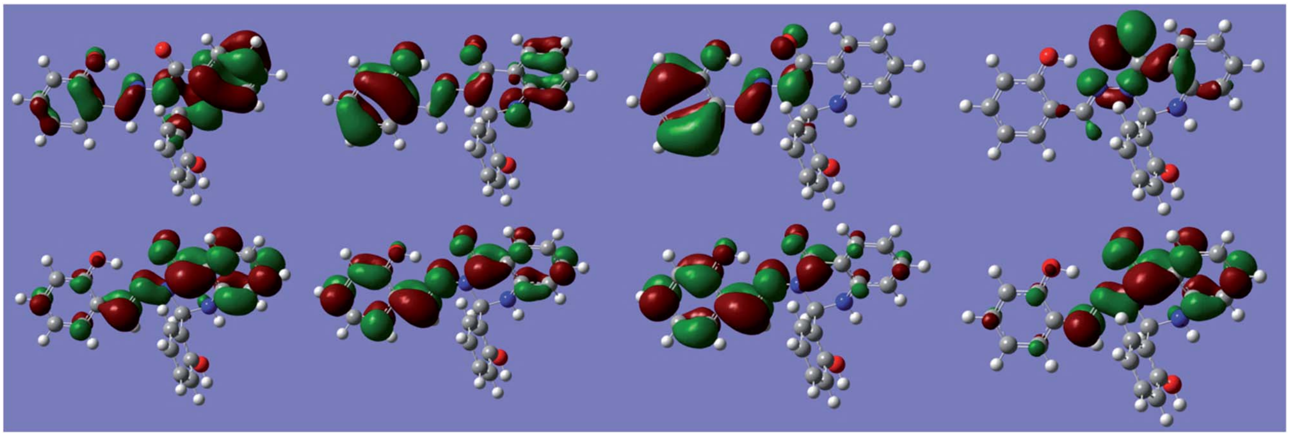

Fig. 12 Natural Transition Orbitals (NTOs) for **S1** at −170° (*anti* minimum). Top: hole orbital. Bottom: excited orbital. Left to right: states ES1 to ES4. Isosurface value: $10^{-1.29}$.

than in the larger. Small model calculations are thus of limited use here; the full π-system needs to be simulated in order to investigate the excited states properly.

4. Conclusions

Experimental and theoretical analysis of the photoswitching behaviour of the N–N linkage in Schiff base (**S1**) possessing a quinazolinone moiety, as well as calculations on model compounds (**M1–M4**), have been performed. UV irradiation (365 nm) caused generation of reactive intermediates of **S1** in DMSO solutions. The formation of radicals (detected by EPR spectroscopy using the spin-trapping technique) resulted from the activation of molecular oxygen by interaction with the excited states of **S1** *via* an electron-transfer process. The activated oxygen molecules further interacted with the DMSO solvent in a series of consecutive reactions to form several spin-adducts, predominantly the $^{\bullet}$DMPO–O_2^- adduct. Other spin-adducts, namely $^{\bullet}$DMPO–OCH_3, $^{\bullet}$DMPO–OR′ and $^{\bullet}$DMPO–CH_3, were detected as well. Subsequent NMR experiments clearly showed formation of the new resonances in high-resolution NMR spectra as the consequence of UV irradiation. The analysis confirmed that these resonances originated from the *syn*-isomer due to isomerization at the N–N linkage. The *anti*- to *syn*-isomerization was relatively fast and the maximum amount of conversion (25%) was detected within 10 min; the thermodynamic equilibrium re-established itself in about 15 min.

Theoretical analysis was performed, involving geometry optimisation at the DFT level (ωB97XD/6-311++G(2d,2p)) and TD-DFT calculations of excited states. Use of a smaller basis set (LANL2DZ) led to qualitatively different energy profiles in some cases. The calculations found the *anti*-form to be lower in energy than the *syn*-form, in accordance with experiment. Isomerization was accompanied by variation of various geometrical parameters, mainly those of or near the C_4–N_3–N_9–C_{10} array. The N_3–N_9 bond length varied by 0.026 Å between the *anti*- and *syn*-forms due to different electron delocalisation in the different forms of **S1**; marked differences in this bond length were seen in the model compounds **M1–M4** as well. The torsion angle C_4–N_3–N_9–C_{10}, whose minima constitute the *syn*- and *anti*-conformers, is affected by the structure and substitution of the molecule in various ways; these have been discussed for **M1–M4** and **S1** and will be further analysed in a future paper.

The excited state energy curves and natural transition orbitals of the excitations differ with size. For the models with minimal π-systems (**M1** and **M2**), the lowest excitation with an appropriate energy profile is an n–π* transition; there are few π*-orbitals due to the minimal π-system, and therefore no π–π* transitions below the n–π* transition. However, the low oscillator strengths of the n–π* transitions would require a route through a π–π* transition and subsequent relaxation. The larger model, **M3**, reproduces the behaviour of the full system (**S1**) reasonably well, in terms of both the ground-state energy curve and the nature of the excited states. For **M3** and **S1**, the 3rd singlet–singlet excitation (π–π*) results in an excited state with an appropriate energy profile for isomerisation; lower excitations are unlikely to be involved.

Conflicts of interest

All authors declare that there are no conflicts of interests.

Acknowledgements

The authors acknowledge financial support from the Slovak Grant Agency VEGA grants no. 2/0022/18 and grant APVV-15-0726. Part of the Gaussian calculations were performed at the Computing Centre of the SAS using the supercomputing infrastructure acquired in projects ITMS 26230120002 and 26210120002, both supported by the Research & Development Operational Program funded by the ERDF. Some calculations (those using OpenMolcas) were performed on the Prašivá cluster of the University of Comenius, Bratislava.

References

1 H. Kandori, Y. Shichida and T. Yoshizawa, *Biochemistry*, 2001, **66**, 1197–1209.
2 C. Dugave, *Cis–trans Isomerization in Biochemistry*, Wiley, Weinheim, Germany, 1st edn, 2006.
3 C. Dugave and L. Demange, *Chem. Rev.*, 2003, **103**, 2475–2532.
4 S. Gozem, H. L. Luk, I. Schapiro and M. Olivucci, *Chem. Rev.*, 2017, **117**, 13502–13565.
5 T. Kumpulainen, B. Lang, A. Rosspeintner and E. Vauthey, *Chem. Rev.*, 2017, **117**, 10826–10939.
6 I. K. Lednev, T.-Q. Ye, P. Matousek, M. Towrie, P. Foggi, F. V. R. Neuwahl, S. Umapathy, R. E. Hester and J. N. Moore, *Chem. Phys. Lett.*, 1998, **290**, 68–74.
7 G. Hegde, A. R. Yuvaraj, W. Sinn-Yam and M. M. Yusoff, *Macromol. Symp.*, 2015, **353**, 240–245.
8 C. Kubli-Garfias, K. Salazar-Salinas, E. C. Perez-Angel and J. M. Seminario, *J. Mol. Model.*, 2011, **17**, 2539–2547.
9 A. R. Yuvaraj, G. S. Mei, A. D. Kulkarni, M. Y. Mashitah, G. Hegde, D. N. Rodríguez and J. M. Otón, *RSC Adv.*, 2014, **4**, 50811–50818.
10 A. Sinicropi, A. Migani, L. De Vico and M. Olivucci, *Photochem. Photobiol. Sci.*, 2003, **2**, 1250–1255.
11 K. P. Rakesh, H. M. Manukumar and D. C. Gowda, *Bioorg. Med. Chem. Lett.*, 2015, **25**, 1072–1077.
12 G. Murtaza, A. Mumtaz, F. A. Khan, S. Ahmad, S. Azhar, M. Najam-Ul-Haq, M. Atif, S. A. Khan, A. Maalik, F. Alam and I. Hussain, *Acta Pol. Pharm.*, 2014, **71**, 531–535.
13 W. Al Zoubi and Y. G. Ko, *Appl. Organomet. Chem.*, 2017, **31**, 1–12.
14 K. M. Abuamer, A. A. Maihub, M. M. El-Ajaily, A. M. Etorki, M. M. Abou-Krisha and M. A. Almagani, *Int. J. Org. Chem.*, 2014, **4**, 7–15.
15 S. M. Borisov, R. Pommer, J. Svec, S. Peters, V. Novakova and I. Klimant, *J. Mater. Chem. C*, 2018, **6**, 8999–9009.
16 W. Al Zoubi, *Int. J. Org. Chem.*, 2013, **03**, 73–95.

17 K. Andiappan, A. Sanmugam, E. Deivanayagam, K. Karuppasamy, H. S. Kim and D. Vikraman, *Sci. Rep.*, 2018, **8**, 1–12.

18 A. Kajal, S. Bala, S. Kamboj, N. Sharma and V. Saini, *J. Catal.*, 2013, **2013**, 1–14.

19 E. Akila, M. Usharani, P. Maheswaran and R. Rajavel, *International Journal of Advanced Scientific and Technical Research*, 2013, **5**, 477–491.

20 D. Chaturvedi and M. Kamboj, *Chem. Sci. J.*, 2016, **7**, e114.

21 E. L. de Araújo, H. F. G. Barbosa, E. R. Dockal and É. T. G. Cavalheiro, *Int. J. Biol. Macromol.*, 2017, **95**, 168–176.

22 G. Grover and S. G. Kini, *Eur. J. Med. Chem.*, 2006, **41**, 256–262.

23 B. Marvania, P. C. Lee, R. Chaniyara, H. Dong, S. Suman, R. Kakadiya, T. C. Chou, T. C. Lee, A. Shah and T. L. Su, *Bioorg. Med. Chem.*, 2011, **19**, 1987–1998.

24 R. A. Smits, M. Adami, E. P. Istyastono, O. P. Zuiderveld, C. M. E. Van Dam, F. J. J. De Kanter, A. Jongejan, G. Coruzzi, R. Leurs and I. J. P. De Esch, *J. Med. Chem.*, 2010, **53**, 2390–2400.

25 I. Khan, S. Zaib, S. Batool, N. Abbas, Z. Ashraf, J. Iqbal and A. Saeed, *Bioorg. Med. Chem.*, 2016, **24**, 2361–2381.

26 N. M. Thong, T. C. Ngo, T. X. N. Phan, D. Q. Dao, T. Van Nam, P. T. T. Trinh and P. C. Nam, *Am. J. Chem.*, 2015, **5**, 91–95.

27 I. G. Ovchinnikova, G. A. Kim, E. G. Matochkina, M. I. Kodess, N. V. Barykin, O. S. Eltsov, E. V. Nosova, G. L. Rusinov and V. N. Charushin, *Russ. Chem. Bull.*, 2014, **63**, 2467–2477.

28 I. G. Ovchinnikova, G. A. Kim, E. G. Matochkina, M. I. Kodess, P. A. Slepukhin, I. S. Kovalev, E. V. Nosova, G. L. Rusinov and V. N. Charushin, *J. Photochem. Photobiol., A*, 2018, **351**, 16–28.

29 E. S. Kelbysheva, L. N. Telegina, T. V. Strelkova, M. G. Ezernitskaya, E. V. Nosova, Y. A. Borisov, B. V. Lokshin and N. M. Loim, *Eur. J. Inorg. Chem.*, 2018, **2018**, 1945–1952.

30 M. Hricovíni and M. Hricovíni, *Tetrahedron*, 2017, **73**, 252–261.

31 C. R. Crecca and A. E. Roitberg, *J. Phys. Chem. A*, 2006, **110**, 8188–8203.

32 K. Bujak, H. Orlikowska, J. G. Małecki, E. Schab-Balcerzak, S. Bartkiewicz, J. Bogucki, A. Sobolewska and J. Konieczkowska, *Dyes Pigm.*, 2019, **160**, 654–662.

33 Z. Hricovíniová, M. Hricovíni and K. Kozics, *Chem. Pap.*, 2017, **72**, 1041–1053.

34 M. J. Frisch, G. W. Trucks, H. B. Schlegel, G. E. Scuseria, M. A. Robb, J. R. Cheeseman, G. Scalmani, V. Barone, B. Mennucci, G. A. Petersson, H. Nakatsuji, M. Caricato, X. Li, H. P. Hratchian, A. F. Izmaylov, J. Bloino, G. Zheng, J. L. Sonnenberg, M. Hada, M. Ehara, K. Toyota, R. Fukuda, J. Hasegawa, M. Ishida, T. Nakajima, Y. Honda, O. Kitao, H. Nakai, T. Vreven, J. A. Montgomery, J. E. Peralta, F. Ogliaro, M. Bearpark, J. J. Heyd, E. Brothers, K. N. Kudin, V. N. Staroverov, R. Kobayashi, J. Normand, K. Raghavachari, A. Rendell, J. C. Burant, S. S. Iyengar, J. Tomasi, M. Cossi, N. Rega, J. M. Millam, M. Klene, J. E. Knox, J. B. Cross, V. Bakken, C. Adamo, J. Jaramillo, R. Gomperts, R. E. Stratmann, O. Yazyev, A. J. Austin, R. Cammi, C. Pomelli, J. W. Ochterski, R. L. Martin, K. Mokoruma, G. Zakrzewski, G. A. Voth, P. Salvador, J. J. Dannenberg, S. Dapprich, A. D. Daniels, Ö. Farkas, J. V. Foresman, J. V. Ortiz, J. Cioslowski and D. J. Fox, *Gaussian 09, Revision D.01*, Gaussian, Inc., Wallingford CT, 2009.

35 J.-D. Chai and M. Head-Gordon, *Phys. Chem. Chem. Phys.*, 2013, **9**, 263–272.

36 T. H. Dunning and J. P. Hay, *Gaussian basis sets for molecular calculations*, Plenum Press, New York, 1977, vol. 3.

37 A. D. McLean and G. S. Chandler, *J. Chem. Phys.*, 1980, **72**, 5639–5648.

38 N. Godbout, D. R. Salahub, J. Andzelm and E. Wimmer, *Can. J. Chem.*, 1992, **70**, 560–571.

39 A. V. Marenich, C. J. Cramer and D. G. Truhlar, *J. Phys. Chem. B*, 2009, **113**, 6378–6396.

40 N. Acar, C. Selçuki and E. Coşkun, *J. Mol. Model.*, 2017, **23**, 1–12.

41 G. D. Purvis and R. J. Bartlett, *J. Chem. Phys.*, 1982, **76**, 1910–1918.

42 J. T. H. Dunning, *J. Chem. Phys.*, 1989, **90**, 1007–1023.

43 R. A. Kendall, T. H. Dunning and R. J. Harrison, *J. Chem. Phys.*, 1992, **96**, 6796–6806.

44 F. Trani, G. Scalmani, G. Zheng, I. Carnimeo, M. J. Frisch and V. Barone, *J. Chem. Theory Comput.*, 2011, **7**, 3304–3313.

45 J. F. Stanton and R. J. Bartlett, *J. Chem. Phys.*, 1993, **98**, 7029–7039.

46 I. F. Galván, M. Vacher, A. Alavi, C. Angeli, F. Aquilante, J. Autschbach, J. J. Bao, S. I. Bokarev, N. A. Bogdanov, R. K. Carlson, L. F. Chibotaru, J. Creutzberg, N. Dattani, M. G. Delcey, S. S. Dong, A. Dreuw, L. Freitag, L. M. Frutos, L. Gagliardi, F. Gendron, A. Giussani, L. González, G. Grell, M. Guo, C. E. Hoyer, M. Johansson, S. Keller, S. Knecht, G. Kovačević, E. Källman, G. Li Manni, M. Lundberg, Y. Ma, S. Mai, J. P. Malhado, P. Å. Malmqvist, P. Marquetand, S. A. Mewes, J. Norell, M. Olivucci, M. Oppel, Q. M. Phung, K. Pierloot, F. Plasser, M. Reiher, A. M. Sand, I. Schapiro, P. Sharma, C. J. Stein, L. K. Sørensen, D. G. Truhlar, M. Ugandi, L. Ungur, A. Valentini, S. Vancoillie, V. Veryazov, O. Weser, T. A. Wesołowski, P. O. Widmark, S. Wouters, A. Zech, J. P. Zobel and R. Lindh, *J. Chem. Theory Comput.*, 2019, **15**, 5925–5964.

47 A. A. Krasnovsky, *Biochemistry*, 2007, **72**, 1065–1080.

48 R. Herscu-Kluska, A. Masarwa, M. Saphier, H. Cohen and D. Meyerstein, *Chem.–Eur. J.*, 2008, **14**, 5880–5889.

49 G. V. Buxton, C. L. Greenstock, W. P. Helman and A. B. Ross, *J. Phys. Chem. Ref. Data*, 1988, **17**, 513–886.

50 M. Hayyan, M. A. Hashim and I. M. Alnashef, *Chem. Rev.*, 2016, **116**, 3029–3085.

51 L. Sobczyk, S. J. Grabowski and T. M. Krygowski, *Chem. Rev.*, 2005, **105**, 3513–3560.

52 L. Vuković, C. F. Burmeister, P. Král and G. Groenhof, *J. Phys. Chem. Lett.*, 2013, **4**, 1005–1011.

53 Y. Wang, Z. Liu, Y. Xu and B. Zhang, *J. Chem. Phys.*, 2015, **143**, 064304.

54 P. J. Coelho, M. C. R. Castro and M. M. M. Raposo, *J. Photochem. Photobiol., A*, 2013, **259**, 59–65.

55 T. Fujino, S. Y. Arzhantsev and T. Tahara, *J. Phys. Chem. A*, 2001, **105**, 8123–8129.

56 H. M. D. Bandara and S. C. Burdette, *Chem. Soc. Rev.*, 2012, **41**, 1809–1825.

57 A. J. Pepino, M. A. Burgos Paci, W. J. Peláez and G. A. Argüello, *Phys. Chem. Chem. Phys.*, 2015, **17**, 12927–12934.

58 Y. C. Lee, P. L. Jackson, M. J. Jablonsky, D. D. Muccio, R. R. Pfister, J. L. Haddox, C. I. Sommers, G. M. Anantharamaiah and M. Chaddha, *Biopolymers*, 2001, **58**, 548–561.

59 E. W.-G. Diau, *J. Phys. Chem. A*, 2004, **108**, 950–956.

60 E. Tajkhorshid, B. Paizs and S. Suhai, *J. Phys. Chem. B*, 1997, **101**, 8021–8028.

61 T. T. Quang, K. P. P. Nguyen and P. E. Hansen, *Magn. Reson. Chem.*, 2005, **43**, 302–308.

62 V. Ferraresi-Curotto, G. A. Echeverría, O. E. Piro, R. Pis-Diez and A. C. González-Baró, *Spectrochim. Acta, Part A*, 2015, **137**, 692–700.

63 P. Suna, P. Hota and P. K. Misra, *Indian J. Chem., Sect. A: Inorg., Bio-inorg., Phys., Theor. Anal. Chem.*, 2016, **55**, 1192–1201.

64 Y. S. Lin, G. De Li, S. P. Mao and J. Da Chai, *J. Chem. Theory Comput.*, 2013, **9**, 263–272.

65 M. Kasha, *Discuss. Faraday Soc.*, 1950, **9**, 14.

66 H. W. Tseng, J. Y. Shen, T. Y. Kuo, T. S. Tu, Y. A. Chen, A. P. Demchenko and P. T. Chou, *Chem. Sci.*, 2016, **7**, 655–665.

67 A. P. Demchenko, V. I. Tomin and P. T. Chou, *Chem. Rev.*, 2017, **117**, 13353–13381.